

Universal Scaling Behaviors of Entangled Polymer Melts at High-stress Shear

Zipeng Xu,¹ Ruikun Sun,¹ Wei Lu,² Jimmy Mays,² and Shiwang Cheng^{1*}

¹Department of Chemical Engineering and Materials Science, Michigan State University, East Lansing, MI 48824, USA

²Department of Chemistry, University of Tennessee, Knoxville, TN 37996, USA

In addition to the terminal flow (the region I) and the shear thinning (the region II), we discover two new flow regions in capillary flow at the wall stress, σ_w , higher than the plateau modulus of the polymer, G_{pl} . The region III violates the empirical Cox-Merz rule with a significantly weaker shear thinning than the region II, and the region IV exhibits unexpected shear thickening. Moreover, the crossover shear rates between the regions II and III, $\dot{\gamma}_w^{II,III}$, and between the regions III and IV, $\dot{\gamma}_w^{III,IV}$, scale with the number of entanglement per chain, $Z = M_w/M_e$, as $\dot{\gamma}_w^{II,III} \sim Z^{-2.0}$ and $\dot{\gamma}_w^{III,IV} \sim Z^{-1.2}$. We attribute the weakening in shear thinning and the emergence of shear thickening to the deformation-induced non-Gaussian stretching of polymers. These observations offer the first experimental quantification of the deformation behaviors of polymer melts at high-stress shear.

Every year, billions of pounds of polymers are processed for various applications in energy, environmental, health, and infrastructure [1,2]. Understanding the flow characteristics of entangled polymers remains one of the central tasks in polymer science [3-5]. Decades of continuous effort yields to a number of constitutive models [3,6], including the transient network model [7-9], the Doi-Edwards tube model [10], the slip-link model [11-13], etc. Specifically, the Graham-Likhtman-McLeish-Milner (GLaMM) model [14] condensed the original Doi-Edwards tube model as well as its major modifications, including the contour length fluctuation (CLF) [15-17], the constraint release (CR) [18-22], and the chain stretching (CS) [14,23,24]. So far, the GLaMM model serves as the foundation for understanding the flow of entangled polymers. Despite the big success of the GLaMM model on the predictions of the flow of entangled polymers at $Wi_R = \dot{\gamma}\tau_R < 1$, many of its predictions on the flow at $Wi_R > 1$ have not been rigorously examined, especially in polymer melts. Here, the $\dot{\gamma}$ is the shear rate and the τ_R is the Rouse time of the polymer. Consequently, fundamental questions, such as how the degree of chain stretching evolves with shear rates as well as its modifications to the characteristics of polymer flow, remain unanswered. For instance, will the highly extended chain conformations observed in polymer solutions [25-29] appear in polymer melt? How will the shear thinning behavior be modified for the entangled polymer flow with highly extended chains?

Experimentally, it is extremely difficult to access the steady-state flow of entangled polymers at $Wi_R > 1$ due to the large torque requirement and the severe edge fracture [30,31]. Previous experiments based on the cone-partition plate (CPP) allowed accessing the steady-state shear up to $Wi_R > 1$ for entangled polymer solutions [32-34]. However, the same strategy cannot be applied to polymer melts. Furthermore, existent experiments on the start-up shear of constant shear rate, $\dot{\gamma}$, were all focused on the steady-state shear stress, σ_s ,

smaller than the plateau modulus, G_{pl} , leaving the case of $\sigma_s > G_{pl}$ largely unexplored. Alternatively, the steady-state shear flow can be achieved in controlled stress experiments. For polymer melts, the σ_s vs $\dot{\gamma}$ from both the controlled strain rate and the controlled stress tests should converge [14,34]. Capillary rheology has been applied to study the shear thinning of entangled polymer melts [35,36], where the empirical Cox-Merz rule holds and the flow curve of the polymer, $\dot{\gamma}_w$ vs σ_w , matches well with the ω vs $G^*(\omega)$ from the linear viscoelastic measurements [37,38]. Here, the $\dot{\gamma}_w$ and σ_w are the shear rate and shear stress at the wall, the $G^*(\omega) = \sqrt{G'(\omega)^2 + G''(\omega)^2}$, and the $G'(\omega)$ and $G''(\omega)$ are the storage and loss modulus of the polymer at angular frequency, ω . However, flow instabilities, such as the wall slip, the stick-slip transition, and the gross melt-fracture, emerge quickly as the applied stress approaches G_{pl} [35]. Therefore, it is highly demanding to develop new strategies to eliminate the flow instabilities and to delineate the characteristics of the fast flow of entangled polymer melts at $\sigma_w > G_{pl}$.

In this Letter, we unravel, for the first time, new scaling behaviors of entangled polymer melt flow at stress up to $\sigma_s > G_{pl}$. By choosing entangled polymer melts with small de Gennes-Brochard slip length [39], b , and collecting flow curves at temperatures not well above their glass transition temperature, T_g , we were able to access polymer flow of high Weissenberg numbers, $Wi_d = \dot{\gamma}\tau_d$, at small $\dot{\gamma}$ before the emergence of flow instabilities. τ_d is the terminal relaxation time of the polymer. Eight polymer melts are included in the study: monodispersed polystyrene (PS) with molecular weight (M_w) of 20 kg/mol, 62 kg/mol, 100 kg/mol, and 311 kg/mol, monodispersed polymethacrylate (PMA) with M_w of 25 kg/mol and 92 kg/mol, monodispersed poly(methyl methacrylate) (PMMA) with M_w of 42 kg/mol, and polydispersed poly(2-vinyl pyridine) (P2VP) with M_w of 100 kg/mol. In the following, we refer to each polymer by their

* Corresponding Author. Email: chengsh9@msu.edu

abbreviations and M_w . For example, PS20K refers to PS with $M_w = 20$ kg/mol. Detailed sample preparations and basic characterizations are described in the supplementary materials (SM), where the slip length of polymers are $b = \frac{\eta_0}{\eta_i} a$ with η_0 the zero-shear viscosity of the polymer, η_i the effective viscosity at the slip layer, and a the thickness of the slip layer [40]. For entangled polymers, the η_i and a are the viscosity and the mesh size of the polymer [41]. The detailed values of b are presented in Table S1 of the SM with $b/D \ll 1$ for all samples. $D = 1.0$ mm is the diameter of the capillary die. Four different dies with $L/D = 0$ (orifice die), 5, 10, and 20 were included in the study, where L is the length of the die land. All dies have an identical entry angle of 90° . The orifice die offers a direct quantification on the total pressure loss at the two die ends, ΔP_e , and agrees well with the end pressure drop from the Bagley correction (Fig. S1 in the SM) [42]. In terms of the laminar flow, the wall stress is $\sigma_w = (P - \Delta P_e)/(4L/D)$ with P the applied pressure, and the apparent shear rate at the wall, $\dot{\gamma}_{app} = \frac{32Q}{\pi D^3}$ with Q the volumetric flow rate of the extrudate [43]. The true shear rate at the wall is $\dot{\gamma}_w = \dot{\gamma}_{app} \left(\frac{3}{4} + \frac{1}{4} \frac{d \ln Q}{d \ln \sigma_w} \right)$. It is worth emphasizing that we focus our discussions on the flow curves, $\dot{\gamma}_w$ vs σ_w , below that have already taken out the entry effects and performed the Rabinowitsch-Weissenberg correction.

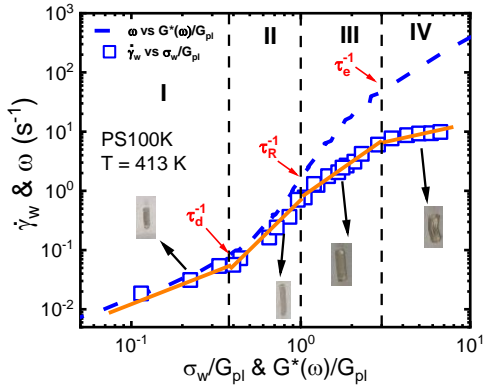


Figure 1. Flow curve of the PS100K (blue squares) and the ω vs $G^*(\omega)/G_{pl}$ (dashed blue lines) at $T = 413$ K. Four flow regions (I-IV) were observed from the different power indexes β of $\dot{\gamma}_w \sim \sigma_w^\beta$. The solid yellow lines are guides for the eye. The Cox-Merz rule only applies to the regions I and II. The inset images are the extrudate at each flow region, indicating the absence of entry instability in the measurements.

Figure 1 presents the flow curve of PS100K (the blue squares) at $T = 413$ K at $\sigma_w/G_{pl} = 0.1 \sim 6$. The dashed blue line represents the outcomes of the Cox-Merz rule of ω vs $G^*(\omega)/G_{pl}$. The inset images show the extrudate at different stages of the flow. Remarkably, the surface of the extrudates is smooth without distortion, indicating the absence of flow instabilities and the validation of the lamellar flow assumption at the stress range of the experiments. Note that the extrudates of PS100K at higher temperatures of $T = 433$ K at $\sigma_w > G_{pl}$ do show strong distortion (Fig. S2 in SM), and the flow curve

at $T = 433$ K at $\sigma_w > G_{pl}$ doesn't match with that of $T = 413$ K, suggesting interesting temperature dependence of the entry instability. Nevertheless, Fig. 1 demonstrates that suppressing the slip length and lowering the testing temperature are effective ways of accessing fast flow in capillary extrusion without invoking entry instabilities.

Four different flow regions can be identified from the different power indexes β of $\dot{\gamma}_w \sim \sigma_w^\beta$. Region I belongs to the terminal flow with $\beta_I \sim 1$, and region II is the shear thinning region with $\beta_{II} > 1$. The crossover between the region I and the region II takes place at $\dot{\gamma}_w^{I,II} \sim \tau_d^{-1}$ and $\sigma_w^{I,II}/G_{pl} \sim 0.3$. The flow curves in regions I and II agree well with the empirical Cox-Merz rule [38]. Interestingly, further increasing the shear stress to $\sigma_w > G_{pl}$ leads to a new region III where significant weakening in shear thinning takes place ($\beta_{II} > \beta_{III} > 1$). As a result, the flow curve deviates from the empirical Cox-Merz rule. Remarkably, another change in the β appears at the shear stress $\sigma_w/G_{pl} \sim 3$ with $\beta_{IV} \sim 0.77 < 1.0$, implying the emergence of shear thickening in the region IV.

While the regions I and II have been well-studied [43], not much have been known about the regions III and IV. The weakening in shear-thinning and the appearance in shear thickening at $\sigma_w/G_{pl} > 1$ and $\sigma_w/G_{pl} > 3$ are especially intriguing. First, the monotonic decreasing in power indexes, $\beta_{II} > \beta_{III} > \beta_{IV}$, implies a progressively weakening in shear thinning and rules out the wall slip as the origin of the regions III and IV. Secondly, the wide-angle x-ray diffraction and the differential scanning calorimetry measurements of the extrudates show no signs of crystallization (data are not shown), suggesting the absence of the flow-induced crystallization in the measurements. Lastly, previous capillary extrusion showed a possibility of the involvement of the glassy dynamics [44,45] that led to a shear thickening close to T_g . However, the measurements in Fig. 1 take place at temperatures 40 K above the $T_g = 373$ K of PS100K, where the segmental dynamics $\tau_\alpha = 11 \mu s \ll 1/\dot{\gamma}_w^{III,IV} = 0.1$ s according to the dielectric measurement (Table. S2 in SM). Thus, it is unlikely that the glassy dynamics play a significant role in the measurements here. To be more conclusive, we measured flow curves of PS100K at different temperatures from 393 K to 413 K. The time-temperature superposition works for flow curves at the entire stress region at $T > 403$ K, further supporting the conclusion of the absence of glassy dynamics in the measurements of flow curves (Fig. S2 in SM). Therefore, the shear thickening in region IV is not from the glassy dynamics.

To elucidate the characteristics of the flow at $\sigma_w > G_{pl}$, we varied the M_w of the PS from 20 kg/mol ($Z = M_w/M_e = 1.5$, Rouse melt) to 311 kg/mol ($Z = 23$, highly entangled polymer melt) in Fig. 2a. Here, Z is the number of entanglement per chain and $M_e = 13.5$ kg/mol is the entanglement molecular weight of PS [41]. Several features were worth noting: (i) The flow curves of PS62K and PS311K show four different flow regions. However, the boundary between the regions II and III of PS62K is not as obvious as that of PS100K and PS311K. (ii) For the Rouse melt PS20K, region II is missing and only

three flow regions can be found, indicating a strong origin of the entanglement dynamics for region II. In addition, the appearance of the region IV in PS20K implies the shear thickening may not be from the entanglement dynamics. (iii) The critical stress among adjacent regions doesn't depend on the M_w of the polymer with $\sigma_w^{I,II}/G_{pl} \sim 0.3$, $\sigma_w^{II,III}/G_{pl} \sim 1.0$, and $\sigma_w^{III,IV}/G_{pl} \sim 3$. (iv) The power indexes β at regions I and IV vary only slightly with M_w s with $\beta_I = 1$ and $\beta_{IV} = 0.72 - 0.77$, in sharp contrast to the strong M_w dependent of the β_{II} and β_{III} . To the best of our knowledge, these results provide the first complete assignment on the different regions of the flow curves and the scaling behaviors at $\sigma_w > G_{pl}$.

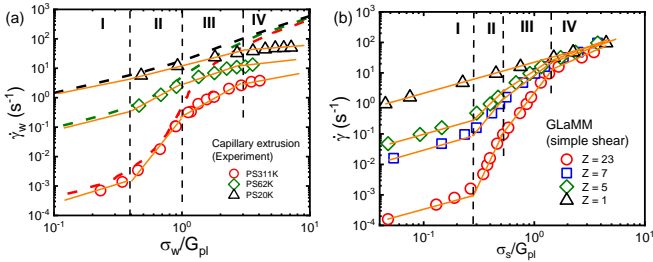


Figure 2. (a) Flow curves of PS20K (black triangles), PS62K (green diamonds), and PS311K (red circles). The dashed lines are the ω vs $G^*(\omega)/G_{pl}$ from small amplitude oscillatory shear measurements. Four different flow regions are visible on PS62K and PS311K. (b) $\dot{\gamma}$ vs σ_s/G_{pl} from the GLaMM model for $Z = 1, 5, 7, \text{ and } 23$, where four flow regions can be identified for $Z > 1$. The solid yellow lines are guides for the eye in both (a) and (b).

In principle, the GLaMM model should be able to predict the flow of highly entangled polymer melts at shear rates up to $\dot{\gamma} > \tau_e^{-1}$ where τ_e is the Rouse time of an entanglement strand. However, the complex geometry of the capillary extrusion makes it a challenging task to perform such calculations for a direct comparison with experiments. However, the goal here is to obtain a qualitative idea of the flow characteristics of the polymer melts at different deformation regions. We thus carried out the GLaMM calculations in the simple shear model. Fig. 2b offers the flow curves, σ_s vs $\dot{\gamma}$, from the GLaMM model on $Z = 1, 5, 7, \text{ and } 23$ with model parameters $c_v = 0.1$ and $R_s = 2.0$ [14] in the simple shear model. $\tau_e = 16$ s is chosen in the calculation to match the high frequency end ($\omega > \tau_e^{-1}$) of linear viscoelastic spectra of PS at $T = 413$ K. It is worth nothing that the chosen of the absolute values of the τ_e doesn't affect the discussions below. Interestingly, the GLaMM model also predicts four distinct flow regions for $Z > 1$ and two flow regions for the Rouse melt with many features consistent with the experiments. According to the GLaMM model, the region I is the terminal flow region with $\sigma_{GLaMM}^{I,II}/G_{pl} \sim 0.3$, $\dot{\gamma}_{GLaMM}^{I,II} \sim \tau_d^{-1}$, and $\beta_{GLaMM}^{I,II} = 1.0$. Region II is the shear thinning region with $\dot{\gamma}_{GLaMM}^{II,III} \sim (\tau_e Z^2)^{-1}$ and $\sigma_{GLaMM}^{II,III}/G_{pl} \sim 0.5 - 0.6$. Since $\dot{\gamma}_{GLaMM}^{II,III}/\dot{\gamma}_{GLaMM}^{I,II} \sim (\tau_e Z^2)^{-1}/\tau_d^{-1} \sim Z^{1.4}$, the GLaMM predicts the scaling of experiments at low stresses. The $(\tau_e Z^2)^{-1} \sim \tau_R^{-1}$ indicates the transition of the regions II and III due to the emergence of the chain stretching.

Furthermore, the GLaMM predicts an M_w independent $\sigma_{GLaMM}^{III,IV}$ and $\dot{\gamma}_{GLaMM}^{III,IV}$ as well as the absence of shear thickening in region IV with $\dot{\gamma}_{GLaMM}^{III,IV} \sim \tau_e^{-1}$, $\sigma_{GLaMM}^{III,IV} \sim G^*(\omega = \tau_e^{-1})$. Therefore, the GLaMM model predicts four flow regions and the scaling of $\dot{\gamma}_w^{II,III}/\dot{\gamma}_w^{I,II} \sim Z^{1.4}$, and it doesn't capture all the characteristics in the regions III and IV. As emphasized previously, we rely on the predictions of the GLaMM for a benchmark of the flow behaviors of the polymer melts at high-stress shear instead of a quantitative comparison between model and experiments.

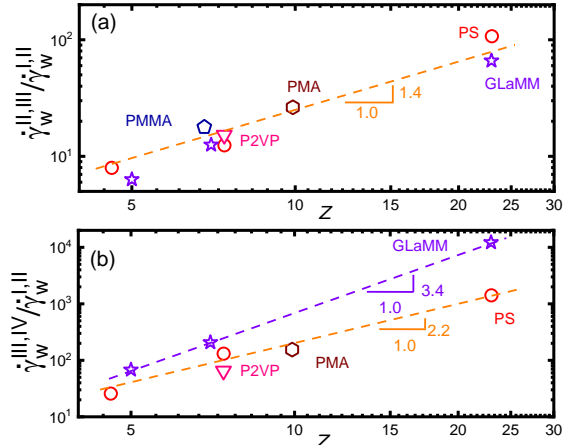


Figure 3 Scaling behaviors between the ratio of the $\dot{\gamma}_w^{II,III}/\dot{\gamma}_w^{I,II}$ and the $\dot{\gamma}_w^{III,IV}/\dot{\gamma}_w^{I,II}$ and the entanglement number per chain, Z , of PS, PMA, PMMA, and P2VP under study. The purple stars represent the predictions from the GLaMM model for simple shear. (a) The $\dot{\gamma}_w^{II,III}/\dot{\gamma}_w^{I,II} \sim Z^{1.4}$ is found in both experiments and the GLaMM model. (b) The $\dot{\gamma}_w^{III,IV}/\dot{\gamma}_w^{I,II} \sim Z^{2.2}$ is found in the experiment and the $\dot{\gamma}_w^{III,IV}/\dot{\gamma}_w^{I,II} \sim Z^{3.4}$ is predicted in the GLaMM model.

To be quantitative, we summarize the scaling of the crossover shear rates between experiments and the GLaMM model in Figures 3a-3b. The GLaMM agrees with experiments on the scaling of $\dot{\gamma}_w^{II,III}/\dot{\gamma}_w^{I,II} \sim Z^{1.4}$ in regions I and II (Fig. 3a). However, the GLaMM predicts a higher scaling index than experiments in regions III and IV with $\dot{\gamma}_w^{III,IV}/\dot{\gamma}_w^{I,II} \sim Z^{3.4}$ (Fig. 3b) instead of the $\dot{\gamma}_w^{III,IV}/\dot{\gamma}_w^{I,II} \sim Z^{2.2}$, indicating a larger influence of the chain stretching in experiments than the predictions of the theory. Note that the GLaMM model assumed a deformed polymer chain adopts the identical tube diameter as the polymer in equilibrium and non-Gaussian stretching of the polymer chain is prohibited [14]. Thus, the strong weakening of shear-thinning in the region III may suggest the presence of non-Gaussian stretching of the polymer chains under high stress. Recent experiments did show evidence on the transient non-Gaussian stretching in the start-up shear of entangled polymers [46] and the possibility of the involvement of intra-chain enthalpic stress [47] for highly stretched polymers, supporting the above conjecture of the non-Gaussian stretching in region III.

Applying the stress beyond $\sigma^{III,IV}$ yields to the remarkable shear thickening in region IV, which further supports the above proposed non-Gaussian stretching mechanism of the polymer chain beyond the region II. The emergence of the

non-Gaussian stretching does not require the presence of entanglement, consistent with the observations of the region IV in Rouse melts (PS20K in Fig. 2a and the PMA25K in Fig. 4a). Intriguingly, the $\dot{\gamma}^{III,IV} \sim \dot{\gamma}^{I,II} Z^{2.2} \sim Z^{-1.2}$ implies the viscosity at the crossover between regions III and IV, $\eta^{III,IV} \sim \sigma^{III,IV} / \dot{\gamma}^{III,IV} \sim Z^{1.2}$. The stronger molecular dependence of $\eta^{III,IV} \sim Z^{1.2}$ than Rouse melts ($\eta \sim Z^1$) even for PS311K ($Z = 23$), suggesting a nearly fully disentanglement state in the shear flow of highly entangled polymer melts at high stress. Previous and recent single-chain visualization experiments [25-29] and computer simulations [48-50] had demonstrated the existence of highly stretched chain conformations in polymer solutions that deviated strongly from the Gaussian chain statistics. Similar highly stretched chain conformation may also exist in pure polymer melt under high-stress shear, which leads to a nearly full disentanglement of the highly entangled polymer melt. Interestingly, such a chain disentanglement state seems to be more resistant to shear than the entangled state and exhibits the unexpected shear thickening according to experiments. Hence, the quantitative understanding of the observed scaling of $\eta^{III,IV} \sim Z^{1.2}$ requires detailed studies on the complex interplay between the intra-chain stress and the inter-chain interaction of the deformation-induced highly stretched entangled polymers. Future computer simulations and small-angle scattering experiments on fast polymer flow should provide more insights into these phenomena.

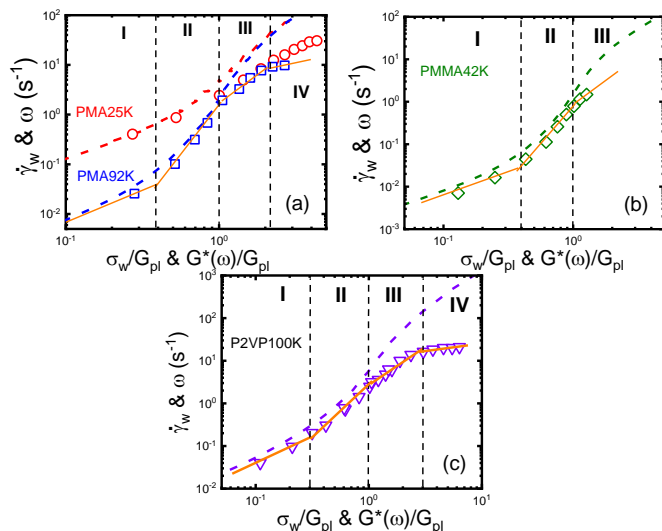


Figure 4. Flow curves of polymers with different polymer chemistry. (a) PMA25K and PMA92K at $T = 323$ K, (b) PMMA42K at $T = 433$ K, (c) P2VP100K at $T = 423$ K. Four flow regions are observed in the PMA92K and P2VP100K. Due to the limitation of the instrument, region IV of the PMMA42K is not accessible. The sample with a high polydispersity index tends to have a blurred boundary between region II and region III. The dashed lines in each panel represent the ω vs $G^*(\omega)/G_{pl}$ of the corresponding polymer at the same testing temperature as the flow curves.

Lastly, we want to comment on the origin of the non-Gaussian chain stretching in regions III and IV. Despite the lack of entry instability in the experiments, the flow field at

the die entry is rather complex and involves elongation flow. The larger die swell ratios of the extrudate from the orifice die than from the normal dies ($L/D = 5$ and 20) at the same volumetric flow rate imply a higher intra-chain deformation at the die entry (Fig. S3 in SM). Thus, the non-Gaussian stretching, if it presents, should be triggered at the die entry and preserved in the die land at the high wall stress. From this perspective, capillary extrusion can serve as an ideal experimental platform to study how the strong chain stretching influences the flow of entangled polymer melts.

To examine the universality of the observed scaling behaviors, we further collected the flow curves of polymers with different polymer chemistry at different temperatures: PMA25K, PMA92K, PMMA42K, and P2VP100K. As shown in Fig. 4, four different flow regions are visible for all polymers except for PMMA42K due to the limited stress window. Interestingly, the boundary between region II and region III is blurred in P2VP100K, which may be due to its high polydispersity index. Besides, the shear thickening is observed in all polymers with different polymer chemistry. Nevertheless, the scaling in shear rates between adjacent flow regions with $\dot{\gamma}_w^{II,III} / \dot{\gamma}_w^{I,II} \sim Z^{1.4}$ and $\dot{\gamma}_w^{III,IV} / \dot{\gamma}_w^{I,II} \sim Z^{2.2}$ remain unchanged with polymer chemistry (Figs. 3a-3b), indicating the universality of the observed scaling behaviors.

In summary, we reported, for the first time, the scaling behaviors of the flow of polymer melt at a high shear stress of $\sigma_s > G_{pl}$. We demonstrated that suppressing the slip length and lowering the testing temperatures can be effective ways of accessing high-stress shear of highly entangled polymer melts up to $\sigma_w/G_{pl} = 6$. Four flow regions have been identified in experiments, where the Cox-Merz rule works only for the regions I and II at $\sigma_w/G_{pl} < 1.0$. Universal scaling behaviors were revealed as $\dot{\gamma}_w^{II,III} / \dot{\gamma}_w^{I,II} \sim Z^{1.4}$ and $\dot{\gamma}_w^{III,IV} / \dot{\gamma}_w^{I,II} \sim Z^{2.2}$ at $\sigma_w/G_{pl} > 1.0$, suggesting unusual roles of the strong chain stretching to the characteristics of polymer flow. We attribute the weakening in shear-thinning in region III and the emergence in shear thickening in region IV to the polymer non-Gaussian stretching at high shear stress, which introduces a complex interplay between the intra-chain and inter-chain stress and leads to the unexpected scaling behaviors in the fast flow of polymer melts. These observations lay down a solid foundation for the fast flow of entangled polymers, and offer crucial insights on the development of next-generation constitutive models of polymer melts.

This work was supported, in part, by Michigan State University. Z. X. acknowledges the financial support from the MSU-ENSURE program. We thank Prof. Graham to share the FORTAN code of the GLaMM model for the calculations in the paper.

[1] L. H. Sperling, *Introduction to Physical Polymer Science* (John Wiley & Sons, Inc., 2005).

[2] *Plastics Market Size, Share & Trends Analysis Report By Product (PE, PP, PU, PVC, PET, Polystyrene, ABS, PBT, PPO, Epoxy Polymers, LCP, PC, Polyamide), By Application, And Segment Forecasts, 2019 - 2025* Report No. 978-1-68038-232-7, 2019.

- [3] R. G. Larson, *Constitutive equations for polymer melts and solutions* (Ed. Butterworth-Heinemann, Boston, 1988).
- [4] J. Bent, L. R. Hutchings, R. W. Richards, T. Gough, R. Spares, P. D. Coates, I. Grillo, O. G. Harlen, D. J. Read, R. S. Graham, A. E. Likhtman, D. J. Groves, T. M. Nicholson, and T. C. B. McLeish, *Science* **301**, 1691 (2003).
- [5] D. J. Read, D. Auhl, C. Das, J. den Doelder, M. Kapnistos, I. Vittorias, and T. C. B. McLeish, *Science* **333**, 1871 (2011).
- [6] R. B. Bird, C. F. Curtiss, R. C. Armstrong, and O. Hassager, *Dynamics of Polymeric Liquids, Volume 2: Kinetic Theory* (Wiley-Interscience, 1987), 2nd edn.
- [7] N. P. Thien and R. I. Tanner, *J. Non-Newtonian Fluid Mech.* **2**, 353 (1977).
- [8] D. Acierno, F. P. Lamantia, G. Marrucci, and G. Titomanlio, *J. Non-Newtonian Fluid Mech.* **1**, 125 (1976).
- [9] H. Giesekus, *J. Non-Newtonian Fluid Mech.* **17**, 349 (1985).
- [10] M. Doi, and S.F. Edwards, *The theory of polymer dynamics* (Oxford University Press, New York, 1986).
- [11] S. F. Edwards and T. Vilgis, *Polymer* **27**, 483 (1986).
- [12] M. Rubinstein and S. Panyukov, *Macromolecules* **35**, 6670 (2002).
- [13] J. D. Schieber, J. Neergaard, and S. Gupta, *J. Rheol.* **47**, 213 (2003).
- [14] R. S. Graham, A. E. Likhtman, T. C. B. McLeish, and S. T. Milner, *J. Rheol.* **47**, 1171 (2003).
- [15] M. Doi, *J. Polym. Sci., Polym. Phys. Ed* **21**, 667 (1983).
- [16] S. T. Milner and T. C. B. McLeish, *Phys. Rev. Lett.* **81**, 725 (1998).
- [17] A. E. Likhtman and T. C. B. McLeish, *Macromolecules* **35**, 6332 (2002).
- [18] M. Daoud and P. G. De Gennes, *J. Polym. Sci., Polym. Phys. Ed* **17**, 1971 (1979).
- [19] G. Marrucci, *J. Non-Newtonian Fluid Mech.* **62**, 279 (1996).
- [20] J. Klein, *Macromolecules* **19**, 105 (1986).
- [21] D. W. Mead, R. G. Larson, and M. Doi, *Macromolecules* **31**, 7895 (1998).
- [22] S. T. Milner, T. C. B. McLeish, and A. E. Likhtman, *J. Rheol.* **45**, 539 (2001).
- [23] G. Marrucci and N. Grizzuti, *Gazz. Chim. Ital.* **118** (1988).
- [24] D. Pearson, E. Herbolzheimer, N. Grizzuti, and G. Marrucci, *J. Polym. Sci., Part B: Polym. Phys.* **29**, 1589 (1991).
- [25] T. Perkins, Quake, D. Smith, and S. Chu, *Science* **264**, 822 (1994).
- [26] T. Perkins, D. Smith, and S. Chu, *Science* **264**, 819 (1994).
- [27] D. E. Smith, H. P. Babcock, and S. Chu, *Science* **283**, 1724 (1999).
- [28] Y. Zhou and C. M. Schroeder, *Phys. Rev. Lett.* **120**, 267801 (2018).
- [29] C. M. Schroeder, R. E. Teixeira, E. S. G. Shaqfeh, and S. Chu, *Phys. Rev. Lett.* **95**, 018301 (2005).
- [30] E. A. Jensen and J. d. Christiansen, *J. Non-Newtonian Fluid Mech.* **148**, 41 (2008).
- [31] E. J. Hemingway, H. Kusumaatmaja, and S. M. Fielding, *Phys. Rev. Lett.* **119**, 028006 (2017).
- [32] E. V. Menezes and W. W. Graessley, *J. Polym. Sci., Polym. Phys. Ed* **20**, 1817 (1982).
- [33] S. Ravindranath and S. Q. Wang, *J. Rheol.* **52**, 957 (2008).
- [34] S. Cheng and S. Q. Wang, *J. Rheol.* **56**, 1413 (2012).
- [35] M. M. Denn, *Annu. Rev. Fluid Mech.* **33**, 265 (2001).
- [36] J. M. Dealy and K. F. Wissbrun, *Melt Rheology and Its Role in Plastics Processing: Theory and Applications* (Springer, 1999).
- [37] W. P. Cox and E. H. Merz, *Journal of Polymer Science* **28**, 619 (1958).
- [38] X. Yang, S.-Q. Wang, A. Halasa, and H. Ishida, *Rheol. Acta* **37**, 415 (1998).
- [39] F. Brochard and P. G. De Gennes, *Langmuir* **8**, 3033 (1992).
- [40] P. P. Drda and S.-Q. Wang, *Phys. Rev. Lett.* **75**, 2698 (1995).
- [41] L. J. Fetters, D. J. Lohse, D. Richter, T. A. Witten, and A. Zirkel, *Macromolecules* **27**, 4639 (1994).
- [42] S. Kim and J. M. Dealy, *J. Rheol.* **45**, 1413 (2001).
- [43] S.-Q. Wang, *Nonlinear Polymer Rheology: Macroscopic Phenomenology and Molecular Foundation* (Wiley, 2017). 480.
- [44] R. C. Penwell and R. S. Porter, *J. Appl. Polym. Sci.* **13**, 2427 (1969).
- [45] A. Casale, R. C. Penwell, and B. S. Porter, *Rheol. Acta* **10**, 412 (1971).
- [46] G. Liu, S. Cheng, H. Lee, H. Ma, H. Xu, T. Chang, R. P. Quirk, and S. Q. Wang, *Phys. Rev. Lett.* **111**, 068302 (2013).
- [47] Z. Zhao, X. Zhao, J. Liu, W. Wang, J. Mays, and S.-Q. Wang, *J. Chem. Phys.* **151**, 124906 (2019).
- [48] R. E. Teixeira, H. P. Babcock, E. S. G. Shaqfeh, and S. Chu, *Macromolecules* **38**, 581 (2005).
- [49] I. Saha Dalal, A. Albaugh, N. Hoda, and R. G. Larson, *Macromolecules* **45**, 9493 (2012).
- [50] I. S. Dalal, N. Hoda, and R. G. Larson, *J. Rheol.* **56**, 305 (2012).

SUPPLEMENTARY MATERIALS

Universal Scaling Behaviors of Entangled Polymer Melts at High-stress Shear

Zipeng Xu, Ruikun Sun, Wei Lu, Jimmy Mays, and Shiwang Cheng
Correspondence should be addressed to Shiwang Cheng (chengsh9@msu.edu)

1. Materials and basic characterizations.

1.1 Materials. Poly(methacrylate) (PMA) and poly(methyl methacrylate) (PMMA) were polymerized through atom-transfer radical-polymerization (ATRP) under high-vacuum conditions (10^{-6} mmHg) in a glass apparatus. Certain amounts (depending on the target molecular weight) of Ethylene bis(2-bromoisobutyrate) (EBIB, Sigma-Aldrich, 97%), Copper(I) bromide (CuBr, Sigma-Aldrich, 99.9999%), Methyl acrylate (MA, Acros Organics, 99%) or Methyl methacrylate (MMA, Aldrich, 99%), Anisole, and N,N,N',N'',N''-pentamethyldiethylenetriamine (PMDETA, Sigma-Aldrich, 99%) were sequentially added to an ampule, which was degassed by three freeze-thaw-evacuate cycles. The ampule was flame sealed under vacuum and immersed in an oil bath at 85 °C for 2-4 days. The polymerization was quenched with liquid nitrogen. The product solution was passed through aluminum oxide (Acros Organics, neutral) column to remove salt, precipitated twice in a large excess of methanol, and vacuum dried overnight. The resulting polymer was characterized by gel permeation chromatography (GPC), ^1H and ^{13}C NMR spectroscopies to confirm the molecular characteristics and purity. The monodispersed polystyrene (PS) with molecular weight (M_w) of 20 kg/mol, 62 kg/mol, 100 kg/mol, and 311 kg/mol, and the polydispersed poly(2-vinyl pyridine) (P2VP) with M_w of 100 kg/mol are all from Scientific Polymer Products, Inc. and used as received. The details of the number average molecular weight, M_n , weight average molecular weight, M_w , and molecular weight distribution, PDI , were listed in table S1 below.

Table S1. Synthesize and characterization of polymers*

Samples	M_n (kg/mol)	M_w (kg/mol)	PDI	M_e (kg/mol)	T_g (K)	a (nm)	Z	b/D
PS20K	18.7	20	1.07	13.5	370	7.65	1.5	3.0e-5
PS62K	57.9	62	1.07	13.5	373	7.65	4.6	1.37e-3
PS100K	95.2	100	1.05	13.5	373	7.65	7.4	6.9e-3
PS311K	296	311	1.05	13.5	373	7.65	23	0.33
PMA25K	22.1	25	1.13	9.26	291	6.07	2.7	1.8e-4
PMA92K	76.7	92	1.20	9.26	293	6.07	9.9	1.47e-2
PMMA42K	32.3	42	1.20	6.17	115	6.7	6.8	4.5e-3
P2VP100K	N/A	100	N/A	13.5	374	7.65	7.4	6.9e-3

* a is the mesh size (the tube diameter) of the polymer according to Ref. [1]. $Z = M_w/M_e$ is the number of entanglement per chain. $b = Z^{3.4}a$ is the de Genne-Brochard slip length of the polymer.

1.2 Linear viscoelastic measurement. Small amplitude oscillatory shear (SAOS) has been performed on an Anton Paar MCR302 rheometer with a CTD600 environmental chamber. The accuracy of the temperature control is ± 0.1 K. A pair of a parallel plate of 8 mm in diameter were applied in all experiments with the frequency range of 10^{-2} - 10^2 rad/s at a strain amplitude of 0.1%. The linear viscoelastic master curves were constructed by the time-temperature superposition principle and the shift factor, a_T , was obtained accordingly. It is worth noting that the shift factor a_T from the SAOS measurement is almost identical to that of the linear creep measurements for the PS samples at the temperature range of 393.15 K to 438.15 K.

1.3 Capillary extrusion. The capillary extrusion was carried out on a pressure-controlled automatic Monsanto capillary rheometer. In the experiment, a pressure was given and the polymer melts in the barrel were extruded out. The volumetric flow rate of the polymer, Q , at a given applied pressure, $P = 0 - 36$ MPa, was obtained through measuring the mass, Δm , of the extrudate for a certain period, Δt : $Q = \frac{\Delta m}{\rho \Delta t}$ with ρ the mass density of the polymer melt. In terms of the laminar flow, the wall stress was, $\sigma_w = (P - \Delta P_e)/(4L/D)$, with ΔP_e the entry pressure loss at the two die

ends, $L = 0 \text{ mm}, 5 \text{ mm}, 10 \text{ mm}, \text{ and } 20 \text{ mm}$ the length of the die land, and $D = 1 \text{ mm}$ the diameter of the die. The ΔP_e can be estimated from the Bagley correction and the orifice die ($L = 0 \text{ mm}$) correction, both of which yield to similar values (see Fig. S1). We applied the orifice die correction for the flow curves in the main content. The apparent shear rate at the wall was $\dot{\gamma}_{app} = \frac{32Q}{\pi D^3}$. The true shear rate at the wall after the Rabinowitsch-Weissenberg correction was $\dot{\gamma}_w = \dot{\gamma}_{app} \left(\frac{3}{4} + \frac{1}{4} \frac{d \ln Q}{d \ln \sigma_w} \right)$. The diameter of the extrudate, D_s , was measured directly after solidified by a caliper with an accuracy $\pm 0.01 \text{ mm}$. Consequently, the die swell ratio was D_s/D (Fig. S3)

1.4 Differential scanning calorimetry. The glass transition temperature, T_g , of polymer melts were determined on a Discovery DSC25 (TA instrument) at the cooling process. The PS, PMMA, and P2VP melts were first heated up to 453 K and annealed for 5 minutes before cooling. The PMA was heated up to 373K and annealed for 5 minutes before cooling. The cooling rate was 10 K/min for all measurements. The T_g was then determined as the inflection point of the glass transition step.

1.5 Dielectric measurements. The segmental relaxation of the PS was measured on a Novocontrol Concept-40 system with an Alpha-A impedance analyzer and a Quatro temperature control system. A PS disk with a thickness of 0.14 mm and a diameter of 14 mm was first filled into a Teflon hollow spacer with the same thickness and hole sizes. The PS thin film with the Telfon spacer was then sandwiched by two gold electrodes with a diameter of 20 mm for dielectric measurements at a frequency range of $10^{-2} - 10^7 \text{ Hz}$ from 438.15 K to 383.15 K. The measurements were performed at an interval of 5 K upon cooling. Thermal equilibrium of 20 minutes was applied before each measurement. The segmental relaxation is estimated as $\tau_\alpha = 1/\omega_p$ with ω_p the peak frequency of

the dielectric loss peak.

2. The end pressure drop from the Bagley correction and the orifice die.

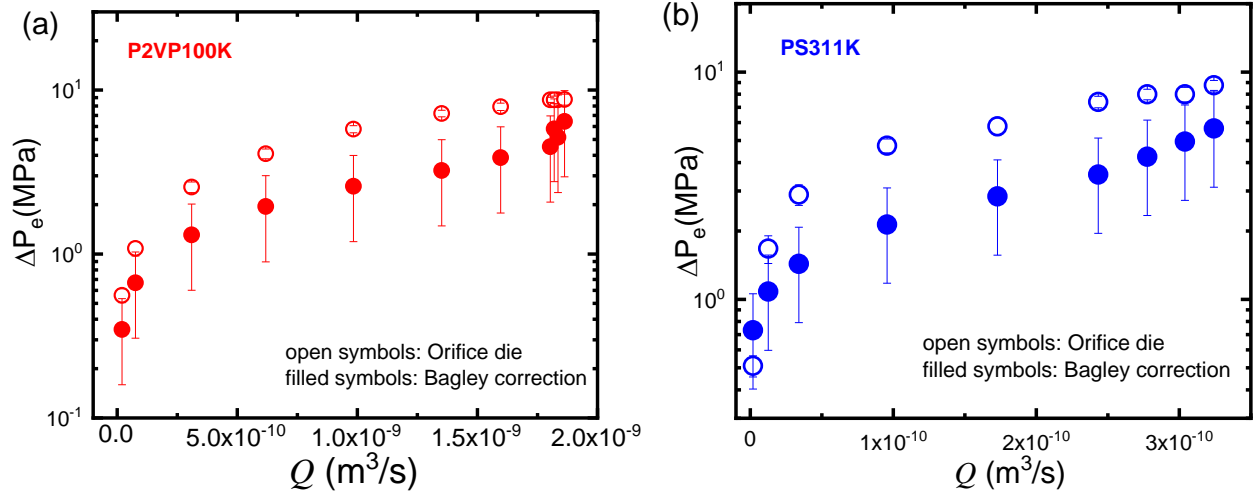


Figure S1. The end pressure drop, ΔP_e , from the measurement of the orifice die (open symbols) and the estimate of the Bagley correction (filled symbols) at the same volumetric flow rate, Q , for (a) polydispersed P2VP100K and (b) monodispersed PS311K. Comparable end pressure drop was observed. In the main content, we adopted the end pressure drop from the direct measurement of the orifice die.

3. Temperature dependence of the flow curves and the extrudate distortion.

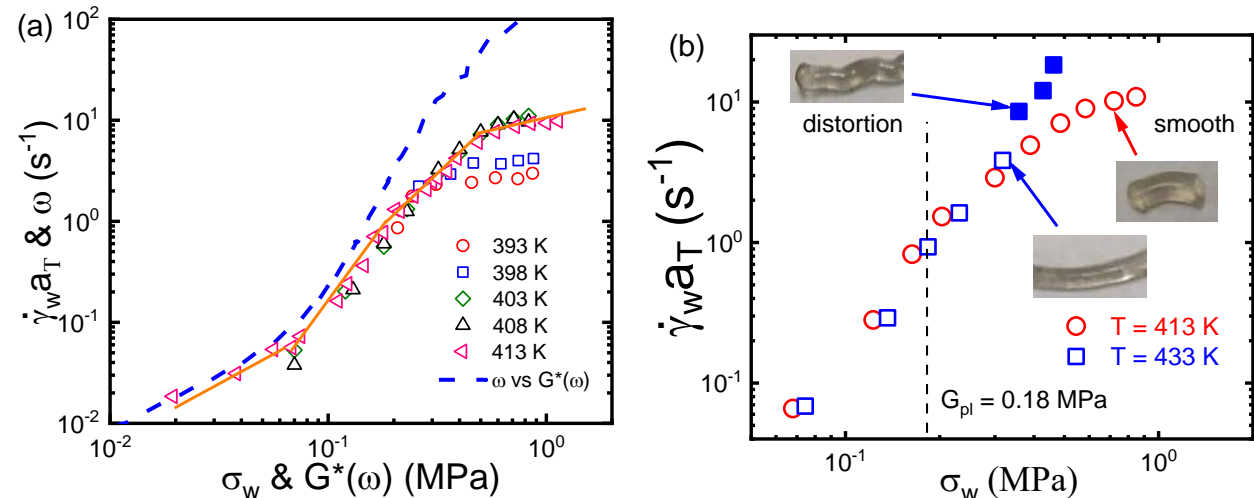


Figure S2. (a) The temperature dependence of the normalized flow curves (after end pressure drop correction), $\dot{\gamma}_w a_T$ vs σ_w , of PS100K at various temperatures from $T = 393$ K to 413 K. The reference temperature is $T = 413$ K. The dashed line is the ω vs $G^*(\omega)$ from the SAOS of the PS100K at $T = 413$ K. (b) The comparison of the normalized flow curves (before end pressure drop correction) of $T = 413$ K and $T = 433$ K, where the strong deviation between the flow curves takes place in the region IV. Moreover, the extrudate at $T = 413$ K is smooth and in the absence of distortion over the whole applied stress range, while the extrudate at $T = 433$ K is significantly

distorted at high stresses. These observations suggest an interesting temperature dependence of the entry instability.

4. Segmental relaxation of the PS100K from dielectric measurements.

Table S2 Segmental relaxation time of PS100K

Temperature (K)	Segmental relaxation time (s)	Temperature (K)	Segmental relaxation time (s)
383.15	0.5655	413.15	1.10259e-5
388.15	0.02377	418.15	4.15912e-6
393.15	0.00246	423.15	1.8485e-6
398.15	4.41035e-4	428.15	7.90388e-7
403.15	1.10259e-4	433.15	3.65823e-7
408.15	3.52828e-5	438.15	1.88304e-7

5. Die swell ratios of the orifice die and the normal dies at the same volumetric flow rates.

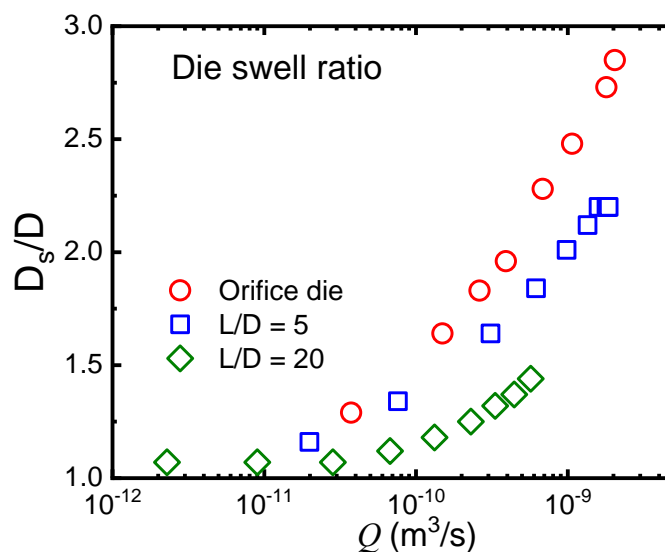


Figure S3. Die swell ratio of the extrudate of P2VP100K at $T = 423$ K with the volumetric flow rate at $L/D = 0$ (orifice die), 5, and 20.

6. Reference:

- [1] L. J. Fetters, D. J. Lohse, D. Richter, T. A. Witten, and A. Zirkel, *Macromolecules* **27**, 4639 (1994).